

Highly Planar Benzodipyrrole-Based Hole Transporting Materials with Passivation Effect for Efficient Perovskite Solar Cells

Cansu Igci, Hiroyuki Kanda, So-Min Yoo, Albertus Adrian Sutanto, Olga A. Syzgantseva, Maria A. Syzgantseva, Vygintas Jankauskas, Kasparas Rakstys, Mounir Mensi, Hobeom Kim,* Abdullah M. Asiri, and Mohammad Khaja Nazeeruddin*

Three benzodipyrrole (BDP)-based organic small molecules with substituted 4-methoxyphenyl (CB-1), 3-fluorophenyl (CB-2), and 3-trifluoromethylphenyl (CB-3) are designed, synthesized, and used as a hole-transporting material (HTM) for perovskite solar cells (PSCs). The electrochemical, optical, thermal, electronic, and optoelectronic properties of the HTMs are characterized to verify their suitability for PSCs. The terminal functional groups of the HTMs having different heteroatoms mainly target effective defect passivation of perovskites. Photoluminescence studies and molecular dynamic simulations reveal that fluorine atoms within CB-2 and CB-3 can contribute to the defect passivation via interaction with Pb of the perovskite. In particular, a highly planar conformation of CB-2 on the perovskite surface can facilitate more efficient hole transfer at the interface. Thus, the PSCs employing CB-2 achieve the highest power conversion efficiency (PCE) of 18.23% while the devices using CB-1 and CB-3 exhibit a lower PCE of 16.78% and 16.74%, respectively. PSCs with the BDP-based HTMs demonstrate excellent long-term storage stability without degradation in their PCEs over 6 months. The highly planar geometry, defect passivation effect, and hydrophobicity of CB-2 show its great potential as an HTM for efficient and stable PSCs.


1. Introduction

Organic–inorganic lead–halide perovskites have attracted tremendous research interest in the photovoltaic community due to their efficient light-harvesting capability, high defect tolerance leading to low exciton binding energy, and long carrier diffusion length, and simple solution fabrication process using low-cost materials.^[1–5] The power conversion efficiency (PCE) of perovskite solar cells (PSCs) has dramatically improved from 3.8% to a certified 25.5% in the past decade with a great effort in the development of new perovskite formula, the optimization of device fabrication, and processing methods.^[6–9] In general, high-performing n-i-p-structured PSCs comprise an electron transport layer (ETL), the perovskite absorber, and a hole transport layer (HTL) stacked in sequence on fluorine-doped tin oxide (FTO), which is completed by deposition of Au. Among the components, the HTL has important roles in efficient hole transport and extraction

from the perovskite layer, simultaneously blocking electrons and directing toward ETL.^[4,10] Moreover, the HTL can effectively

C. Igci, H. Kanda, S.-M. Yoo, A. A. Sutanto, M. Mensi, H. Kim, M. K. Nazeeruddin
Institute of Chemical Sciences and Engineering
École Polytechnique Fédérale de Lausanne
CH-1951 Sion, Switzerland
E-mail: hobeom.kim@epfl.ch; mdkhaja.nazeeruddin@epfl.ch

O. A. Syzgantseva, M. A. Syzgantseva
Department of Chemistry
Lomonosov Moscow State University
Moscow 119991, Russia

 The ORCID identification number(s) for the author(s) of this article can be found under <https://doi.org/10.1002/solr.202100667>.

© 2021 The Authors. Solar RRL published by Wiley-VCH GmbH. This is an open access article under the terms of the Creative Commons Attribution License, which permits use, distribution and reproduction in any medium, provided the original work is properly cited.

DOI: 10.1002/solr.202100667

V. Jankauskas
Institute of Chemical Physics
Vilnius University
Vilnius 10257, Lithuania

K. Rakstys
Department of Organic Chemistry
Kaunas University of Technology
Kaunas 50254, Lithuania

A. M. Asiri
Center of Excellence for Advanced Materials Research (CEAMR)
King Abdulaziz University
P.O. Box 80203, 21589 Jeddah, Saudi Arabia

protect the underlying perovskite layer from moisture, oxygen, and the diffusion of the metal electrode.^[11–13] In this regard, the development of new organic hole-transporting materials (HTMs) has received great attention and a significant number of organic HTMs have been introduced.^[14–16] Organic small molecule 2,2',7,7'-tetrakis(*N,N*-di-*p*-methoxyphenylamine)-9,9'-spirobifluorene (spiro-OMeTAD) is the most commonly used HTM to date based on its excellent hole-transporting properties.^[17,18] Nevertheless, it is crucial to continue to design new organic HTMs with improved material properties that can achieve more efficient and stable PSCs and provide a better understanding of the relationship between the HTMs and the device performance.

Benzodipyrrole (BDP) is a pyrrole-based heterocyclic small molecule, and there has been interest in the BDP-based organic molecules for application in organic field-effect transistors (OFETs) and organic light-emitting diodes (OLEDs) as a hole injection material.^[19–22] However, the use of the BDP-based HTMs in PSCs has rarely been studied.^[23,24] The presence of the heteroatom in the BDP core can facilitate the intermolecular non-covalent interaction and increase the molecular planarity while extending π -electron delocalization along the molecular backbone, which can enhance the charge transport properties.^[25–29] In addition, a tunable energy level of the BDP unit is promising to design a well-aligned energy level with perovskites, which can further promote hole extraction.^[25] Moreover, the functionalization of the BDP unit with the heteroatom integration can target effective defect passivation of perovskites resulting in a reduced charge recombination loss, thereby improving device performance.^[30–32]

Herein, we developed three novel BDP-based organic small molecules as a HTM in PSCs, 1,5-dihexyl-2,6-bis(4-methoxyphenyl)-1,5-dihydropyrrolo[2,3-*f*]indole, 2,6-bis(3-

fluorophenyl)-1,5-dihexyl-1,5-dihydropyrrolo[2,3-*f*]indole, and 1,5-dihexyl-2,6-bis(3-(trifluoromethyl)phenyl)-1,5-dihydropyrrolo[2,3-*f*]indole named CB-1, CB-2, and CB-3, respectively (Figure 1). 4-Methoxyphenyl, 3-fluorophenyl, and 3-trifluoromethylphenyl functional groups were attached in the BDP-based HTM structure to examine the heteroatom effects on PSC performance. We investigated the HTMs in terms of electrochemical energy levels, optical properties of absorption and photoluminescence (PL), thermal stability, and electronic properties of hole mobility and film conductivity. Furthermore, molecular dynamic (MD) simulations revealed an interaction between the heteroatoms of the molecules and Pb atom of the perovskite, which proves an impact of the HTMs on the defect passivation effect. We employed the HTMs to fabricate PSCs and the use of CB-2 achieved the highest PCE of 18.23% mainly based on its strong defect passivation effect and intermolecular interaction owing to a high degree of molecular planarity. Meanwhile, the use of CB-1 and CB-3 resulted in a lower PCE of 16.78% and 16.74%, respectively, mainly due to the absence of the passivation effect of CB-1 and the inferior hole-transporting capability of CB-3 despite its defect passivation effect. Finally, we demonstrated significantly stable device performance during long-term storage using the HTMs with improved hydrophobicity, particularly in fluorinated CB-2 and CB-3 HTMs-based PSCs.

2. Results and Discussion

In the molecular design of the HTMs, the alkylated BDP core was preserved as a donor unit while functional groups were modulated with 4-methoxyphenyl, 3-fluorophenyl, and 3-trifluoromethylphenyl for CB-1, CB-2, and CB-3, respectively (Figure 1).

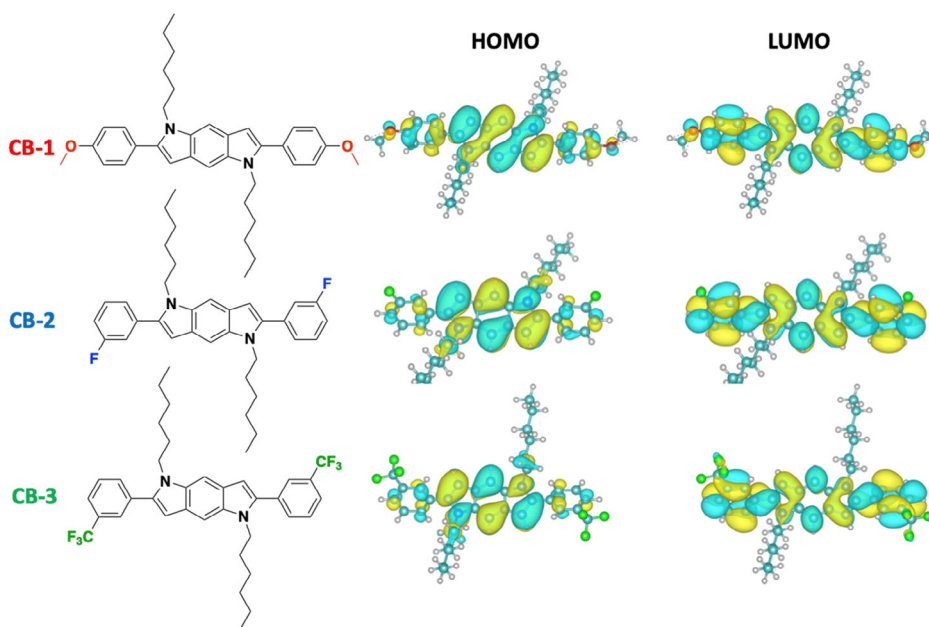


Figure 1. Molecule structure and spatial distribution of HOMO and LUMO orbitals in CB-1, CB-2, and CB-3, computed with PBE-D3 density functional on top of PBE-D3 optimized geometry (isosurface value = 0.015). C, O, N, H, and F atoms are colored in cyan, red, blue, white, and green.

The solubility of the compounds was adjusted by adding long *N*-alkyl chains in the BDP unit, which improve hydrophobicity and solubility in an organic solvent, thus making the HTM solution-processable and protecting perovskite from degradation by moisture.^[14,33] The methoxyphenyl substitution in the CB-1 was chosen due to the electron-donating effect to adjust the highest occupied molecular orbital (HOMO) level and to improve the hole mobility of the HTM layer.^[34] CB-2- and CB-3-containing fluorine atoms have been employed to decrease the lowest unoccupied molecular orbital (LUMO) levels without causing strong steric hindrance, enhance inter/intramolecular non-covalent interactions, and increase hydrophobicity leading to a long-term stability.^[35,36] The three novel BDP-based HTMs were successfully synthesized in a good overall yields. The complete synthetic route and detailed experimental procedure are described in the Supporting Information. Synthesis of the intermediate 2,5-dibromobenzene-1,4-diamine (4) was accomplished starting from commercially available and inexpensive precursor 2,5-dibromoaniline according to the method reported by Moroni et al. with a small modification.^[37] Then, compound (4) was sequentially substituted with *n*-hexyl chains to obtain 2,5-dibromo-*N*¹, *N*⁴-dihexylbenzene-1,4-diamine (5) following by a Sonogashira coupling reaction using PdCl₂(PPh₃)₂, CuI and PPh₃ with 1-ethynyl-4-methoxybenzene, 1-ethynyl-3-fluorobenzene, and 1-ethynyl-3-(trifluoromethyl)benzene units, respectively. Then, zinc-mediated intramolecular cyclization reaction was performed first deprotonating with *n*-BuLi following by transmetalation using ZnCl₂, and completed by quenching the reaction mixture with water. Purification of the final compounds was performed by column chromatography without the need for high-pressure vacuum distillation. The synthesized chemical structures were verified by ¹H and ¹³C NMR spectroscopy and mass spectrometry (Figure S1–S9, Supporting Information). All the final compounds are well-soluble in common organic solvents such as tetrahydrofuran (THF), chloroform, toluene, and chlorobenzene, typically used for HTM processing on perovskite absorbers.

To investigate the energy levels and spatial distribution of frontier orbitals of CB-1, CB-2, and CB-3, the density functional theory (DFT) calculations were carried out, and the benchmarking of the different density functionals was performed (Figure 1). The molecular structures were optimized by using either the PBE-D3 density functional or the hybrid PBE0 density functional, and the HOMO and LUMO energies were calculated by using PBE-D3, B3LYP, and PBE0 density functionals (Table S1, Supporting Information). The obtained orbital energy values correlated well with each other, and the same trend was observed for all cases: $E_{\text{HOMO}}(\text{CB-1}) > E_{\text{HOMO}}(\text{CB-2}) > E_{\text{HOMO}}(\text{CB-3})$ and $E_{\text{LUMO}}(\text{CB-1}) > E_{\text{LUMO}}(\text{CB-2}) > E_{\text{LUMO}}(\text{CB-3})$. When the BDP core is functionalized with electron-donating methoxyphenyl unit in CB-1, the positive mesomeric effect of the methoxy side group increased the electron density in the benzene ring and expanded the conjugation in the molecule, resulting in a higher HOMO/LUMO level. In addition, the trifluoromethylphenyl group of CB-3 has a stronger electron-withdrawing group than the fluorophenyl group of CB-2, which produced the negative inductive effect of CB-3 with deeper HOMO/LUMO levels. The molecular orbital spatial distribution of HOMO and LUMO were similar for all molecules. The

electron density in the HOMO of CB-1, CB-2, and CB-3 was primarily distributed on the BDP unit while that of LUMO was spread along the entire molecule. These results hint that the planar structural geometry of the molecules may be the cause of the larger extent of the orbital delocalization and better conjugated system.^[38]

We performed cyclic voltammetry with a standard three-electrode configuration to experimentally investigate HOMO energies of CB-1, CB-2, and CB-3 (Figure 2a). The materials were tested in dichloromethane containing 0.1 M *n*-Bu₄NPF₆ as a supporting electrolyte and the oxidation potential was calibrated against ferrocene internal standard. The E_{HOMO} values were calculated to be -5.24 , -5.30 , and -5.34 eV versus vacuum for CB-1, CB-2, and CB-3, respectively, showing the same trend with the result of DFT calculation. The HOMO levels are well aligned with the valence band energy level of the typical lead iodide-based perovskites so that the photogenerated charge carriers are efficiently transferred at the interface.^[14]

The optical properties of the molecules were investigated by ultraviolet-visible (UV-Vis) absorption and PL spectroscopy in DCM solutions (Figure 2b). The absorption spectra of the HTMs showed two intense bands in the region of 240 and 340 nm. The first absorption band for CB-1, CB-2, and CB-3 originated from the localized aromatic π - π^* transition of the conjugation system and center at 247, 244, 235 nm, respectively. The strong absorption bands at 333, 336, and 338 nm, respectively of CB-1, CB-2, and CB-3 were ascribed to n - π^* transition. All molecules showed a shoulder-like transition around 400 nm, which may be due to the extension of π -conjugation because of additional phenyl units.^[19] The PL emission peaks of CB-1, CB-2, and CB-3 are centered at 440, 447, and 455 nm, respectively. The optical bandgap (E_g) values, estimated from the corresponding intersections of absorption and emission onsets, were determined to be 398, 410, and 415 nm, which corresponds to E_g of 3.12, 3.02, and 2.99 eV, respectively. The redshift both in the absorption and PL spectra can be attributed to the electron-withdrawing of F in CB-2 and CF₃ in CB-3, which resulted in narrow E_g and lower LUMO level to -2.28 and -2.35 eV, respectively, while CB-1 is -2.12 eV. The large offset between the LUMO of the HTMs and the conduction band energy of the perovskite can effectively block the back-electron transfer. A schematic of the energy band diagram is shown in Figure 2c. All electrochemical, optical, and thermal properties of the materials are summarized in Table 1. To confirm the thermal stability of the new HTMs, we performed thermogravimetric analysis (TGA) recorded under the nitrogen atmosphere at the heating rate of 10 °C min⁻¹. The decomposition temperatures (T_d) determined at 5% weight loss of CB-1, CB-2, and CB-3 were 337, 302, and 251 °C, respectively, indicating that the new HTMs have good thermal stability (Figure S10, Supporting Information).

To investigate charge transport and hole collection properties of the BDP-based HTMs, the xerographic time-of-flight (XTOF) method was used (Figure S11, Supporting Information). Samples were prepared under drop casting technique on Al-coated glass plates using chlorobenzene as a solvent with 0.54–1.2 μm film thickness. The room temperature zero-field hole-drift mobility (μ_0) of CB-1, CB-2, and CB-3 was measured to be $1.1 \times 10^{-5} \text{ cm}^2 \text{ V}^{-1} \text{ s}^{-1}$, $0.63 \times 10^{-5} \text{ cm}^2 \text{ V}^{-1} \text{ s}^{-1}$, and

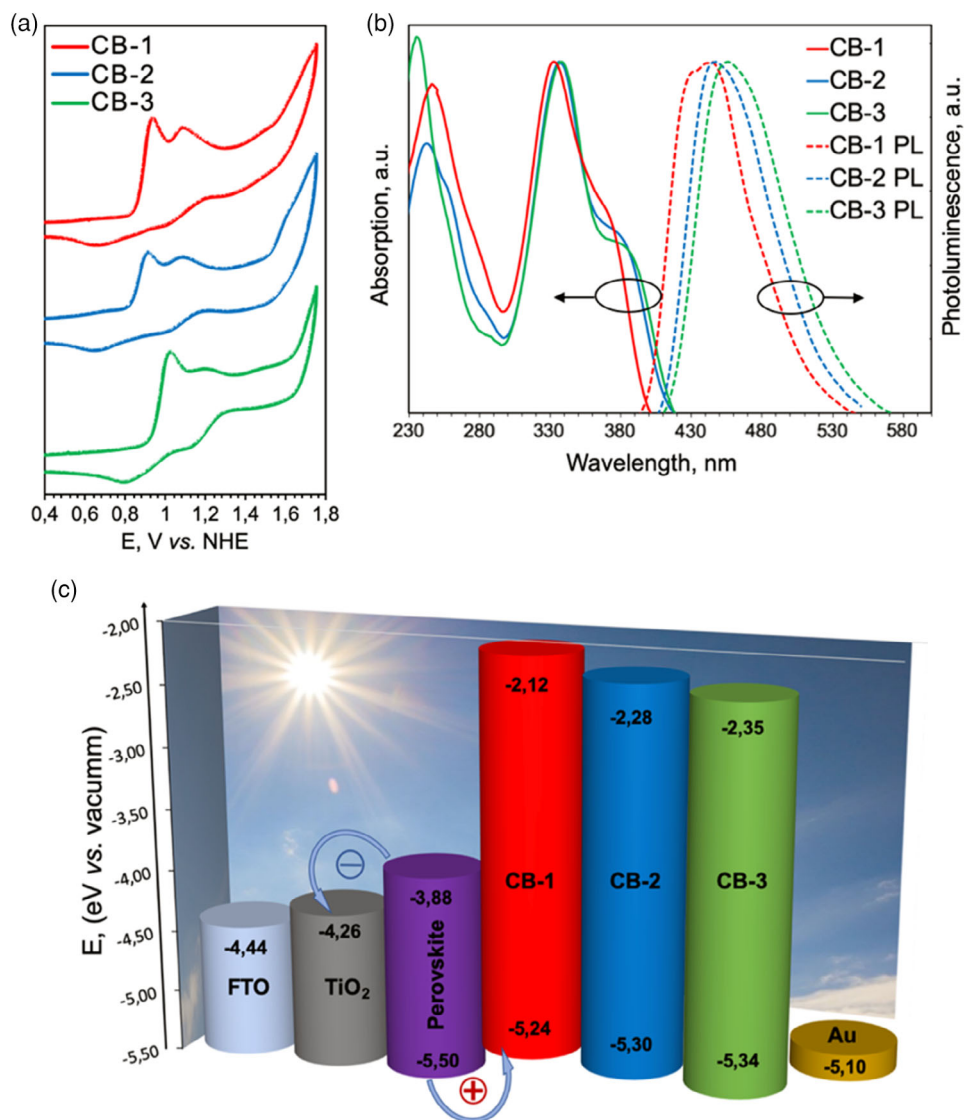


Figure 2. a) Cyclic voltammograms of the HTMs in DCM solution. b) Normalized UV-Vis absorption and PL spectra of BDP-based HTMs in DCM solution. c) Schematic energy level diagram of components used in the devices.

Table 1. Thermal, optical, electrochemical, and electronic properties of CB-1, CB-2, and CB-3.

| HTM | T_d [°C] ^{a)} | λ_{abs} [nm] ^{b)} | λ_{em} [nm] ^{b)} | HOMO [eV] ^{c)} | LUMO [eV] ^{d)} | ΔE_g [eV] ^{e)} | σ [S cm ⁻¹] ^{f)} | μ_0 [cm ² V ⁻¹ s ⁻¹] ^{g)} |
|------|--------------------------|---|--|-------------------------|-------------------------|---------------------------------|--|--|
| CB-1 | 337 | 247, 333 | 440 | -5.24 | -2.12 | 3.12 | 4.72×10^{-4} | 1.1×10^{-5} |
| CB-2 | 302 | 244, 336 | 447 | -5.30 | -2.28 | 3.02 | 4.06×10^{-4} | 0.63×10^{-5} |
| CB-3 | 251 | 235, 338 | 455 | -5.34 | -2.35 | 2.99 | 1.58×10^{-4} | 0.56×10^{-5} |

^{a)}Decomposition temperature corresponding to 5% weight loss determined from TGA; ^{b)}Absorption and emission spectra measured in dichloromethane; ^{c)}Measured in 0.1 M *n*-Bu₄NPF₆/DCM solution using glassy carbon working electrode, Pt reference electrode and Pt counter electrode calibrated by Fc/Fc⁺ as an external reference. Potentials were converted to the normal hydrogen electrode (NHE) by addition of +0.624 and -4.44 eV to the vacuum, respectively; ^{d)}LUMO = HOMO + ΔE_g ; ^{e)} $\Delta E_g = 1240/\lambda_{\text{onset}}$; ^{f)}Conductivity values; ^{g)}Mobility values at zero field strength.

$0.56 \times 10^{-5} \text{ cm}^2 \text{ V}^{-1} \text{ s}^{-1}$, respectively. XTOF transients and the integral XTOF measurements of the samples are detailed in the Supporting Information Figures S12 and S13. Among

the HTMs, CB-1 exhibited a higher hole mobility than that of CB-2 and CB-3, which can be attributed to a higher degree of conjugation and better intermolecular interaction of the

molecule.^[39,40] In addition, lateral thin-film conductivity of the HTMs was measured with OFETs (Figure S14, Supporting Information).^[41] Similar to the result of the hole mobility measurement, CB-1 showed a higher conductivity ($4.72 \times 10^{-4} \text{ S cm}^{-1}$) than CB-2 ($4.06 \times 10^{-4} \text{ S cm}^{-1}$) and CB-3 ($1.58 \times 10^{-4} \text{ S cm}^{-1}$). The conductivity of the doped spiro-OMeTAD as a reference was determined to be $6.25 \times 10^{-4} \text{ S cm}^{-1}$. The results of the hole-mobility and conductivity measurements are summarized in Table 1.

As the film morphology of an HTM is of great importance to realize efficient charge transfer, we performed scanning electron microscopy (SEM) to investigate surface morphology of the HTMs on a perovskite film [(FAPbI₃)_{0.87}(MAPbBr₃)_{0.13}]_{0.92}(CsPbI₃)_{0.08}, which we used as a light absorber of PSCs (Figure 3a). CB-1 presented a highly well-oriented fibril-like structure with sparsely distributed aggregates. The highest hole mobility and conductivity of CB-1 can be attributed to the fiber-like structure, but the microscopic aggregates and the pinholes on the film can obstruct charge carriers to be efficiently collected to the top electrode in PSCs. On the other hand, CB-2 exhibited more homogeneous layer formation than CB-1. Although the microscopic surface morphology of CB-3 looks homogeneous, we found the deposition of CB-3 yielded noticeable macroscopic aggregates on the surface, which can act as non-radiative recombination sites, and negatively impact the device performance (Figure S15, Supporting Information). The control film using Spiro-OMeTAD exhibited a uniform coverage on top of the perovskite layer (Figure S16, Supporting Information). In addition, atomic force microscopy (AFM) measurements were

performed to understand better the morphology of the HTM layers (Figure S17, Supporting Information). The CB-1 film exhibited a nanofibrillar morphology and presented root mean square (RMS) roughness of 16.7 nm, while CB-2 and CB-3 resulted in the RMS roughness of 22.9 and 23.8 nm, respectively.

We investigated PL characteristics of the HTM-deposited perovskite films, which can give insights about charge-carrier dynamics that can closely link to the hole transfer as well as defect state of the perovskite (Figure 3b). For steady-state PL measurements, the films were excited with 475 nm light. The bare perovskite film showed a PL emission peak at 767 nm with the highest intensity.^[42] The deposition of the HTMs on top of the perovskite resulted in a strong quenching of the PL emission compared to the bare perovskite film, indicating the effective hole transfer from the perovskite to the HTMs. The stronger PL quenching upon the deposition of CB-1 than CB-2 and CB-3 implies that more efficient hole transfer can occur at the interface with the use of CB-1. On the other hand, the deposition of CB-2 or CB-3 on the perovskites resulted in a less strong quenching of the PL emission. While the PL quenching can occur due to the efficient hole extraction from the perovskites to an HTM, defects in perovskites can also lead to the PL quenching due to non-radiative recombination of charge carriers. Especially, undercoordinated Pb²⁺ in the perovskites can significantly influence charge-carrier dynamics acting as a non-radiative recombination center.^[35] Nevertheless, the defects can be effectively passivated by fluorine of CB-2 or trifluoromethyl of CB-3, which can suppress the PL quenching.^[43–45] To gain a better understanding, we also performed time-resolved

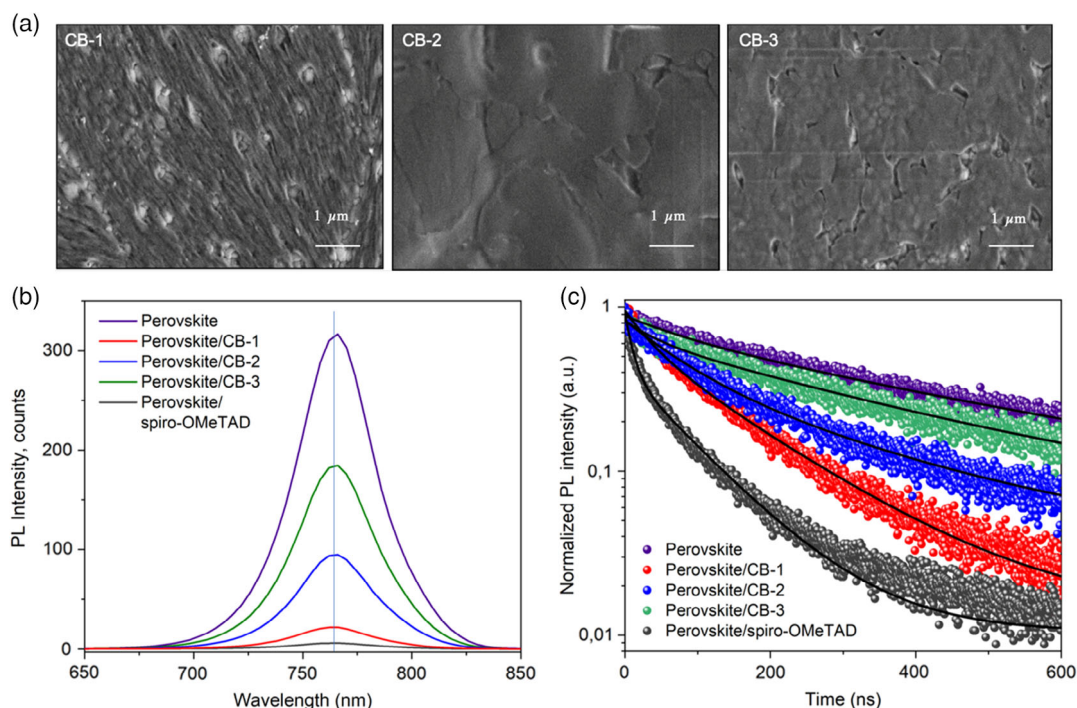


Figure 3. a) Top surface SEM images of HTMs on perovskite. b) Steady-state PL spectra of the pristine perovskite and perovskite/HTM films (CB-1, CB-2, CB-3, and spiro-OMeTAD) upon excitation at 475 nm. c) Transient PL spectra in the first 600 ns time window of the pristine perovskite and perovskite/HTM films upon excitation at 640 nm.

PL (TrPL) measurements of the films, which were excited by 640 nm light. For the neat perovskite film, the PL decay curve was fitted to a mono-exponential decay function, which resulted in the PL lifetime as 338.4 ns (Figure 3c). Meanwhile, the decay curves of the perovskites with HTMs were fitted to a bi-exponential decay function composed of fast-decay (τ_1) and slow-decay component (τ_2), which takes account of non-radiative recombination at the interface and radiative recombination in bulk, respectively.^[46] We summarized the detailed PL lifetime parameters in Table S2, Supporting Information. The average PL lifetime (τ_{ave}) of the films with the HTMs exhibited the same trend to the result of the steady-state PL intensity of the films. The PL lifetime of the neat perovskite film was significantly decreased upon the deposition of CB-1, CB-2, CB-3, and spiro-OMeTAD resulting in $\tau_{ave} = 105.9, 166.3, 263.1,$ and 46.0 ns, respectively, indicating the efficient hole transfer from the perovskite to the HTMs. Meanwhile, the suppressed PL quenching and the retarded PL decay of the films with CB-2 and CB-3 can be attributed to the defect passivation based on an interaction between the fluorine of CB-2 or CB-3 and the undercoordinated Pb^{2+} in the perovskite, which can reduce the non-radiative charge carrier loss at the perovskite interface.^[32]

To obtain more insight into the interface and the passivation effect, first-principles Born–Oppenheimer MD simulations have been performed (Figure 4). In the computational experiments, the HTMs were placed on the perovskite surface and allowed to interact at 300 K constant temperature. While CB-1 did not have a specific interaction with the perovskite, the fluorine atom of CB-2 exhibited a strong interaction with the Pb atoms at the perovskite surface. Therefore, the undercoordinated Pb^{2+} in the perovskite can be effectively passivated by CB-2, leading to the higher intensity and the longer lifetime of PL of the films

than those using CB-1.^[44,47–49] Meanwhile, in addition to BDP core planarity, the geometry of CB-2 also allowed for realization of the benzene rings conformation parallel to the perovskite surface, resulting in a higher planar molecular orientation of CB-2 than CB-1. The distribution of dihedral angles between BDP core and substituted phenyl units along the MD trajectory was analyzed according to occurrences percentage of CB-1, CB-2, and CB-3 (Figure S18, Supporting Information). CB-2 revealed a higher occurrence at smaller dihedral angle between 20° and 40° than CB-1 (40° – 60°) and CB-3 (60° – 80°), as the fluorine atom did not produce a steric hindrance for the rotation of the benzene in the presence of hexyl chains. The higher planarity and smaller dihedral angles of CB-2 may allow better intermolecular π – π stacking of HTM, resulting in a better hole transfer capacity.^[30] On the other hand, the greater number of fluorine atoms of CB-3 also favored the strong interaction with the Pb atoms in the perovskite that gave rise to the highest intensity and the longest lifetime of PL among the use of the three HTMs. But unlike CB-2, the benzene rings of CB-3 systematically have an out-of-plane orientation with respect to the perovskite surface, resulting in a reduced planarity of the molecular configuration with a higher dihedral.

We employed the three BDP-based HTMs to fabricate PSCs consisting of FTO/compact TiO_2 (c- TiO_2)/mesoporous TiO_2 (mp- TiO_2)/ SnO_2 /perovskite [(FAPbI₃)_{0.87}(MAPbBr₃)_{0.13}]_{0.92}(CsPbI₃)_{0.08}]/HTM/ Au. We observed the device structure via cross-sectional SEM, which confirmed the formation of ≈ 70 nm-thick HTLs (Figure S19, Supporting Information). Among the HTMs, CB-2 resulted in the best-performing PSCs having a PCE of 18.23%, open-circuit voltage (V_{oc}) of 1.025 V, short-circuit current (J_{sc}) of 23.19 mA cm^{-2} , and fill factor (FF) of 0.767 in a champion device while the device using

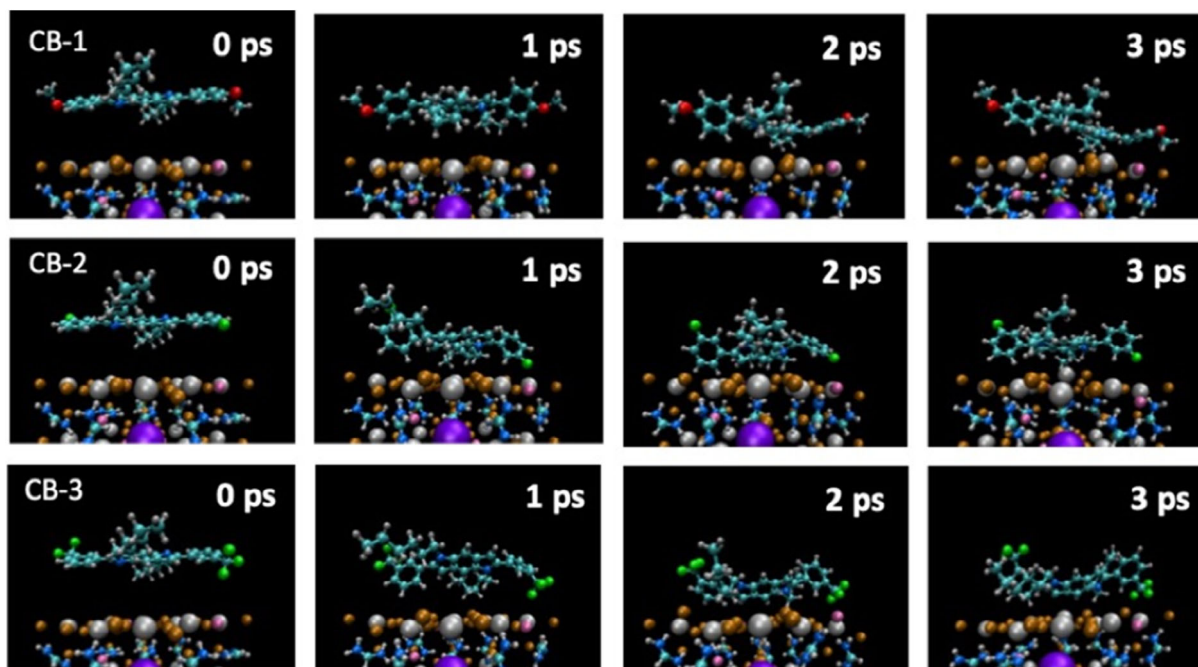


Figure 4. Interaction of CB-1 (top), CB-2 (middle), and CB-3 (bottom) HTMs with perovskite surface. C, O, N, H, F, Br, I, Pb, and Cs atoms are colored in cyan, red, blue, white, green, mauve, brown, grey, and purple, respectively.

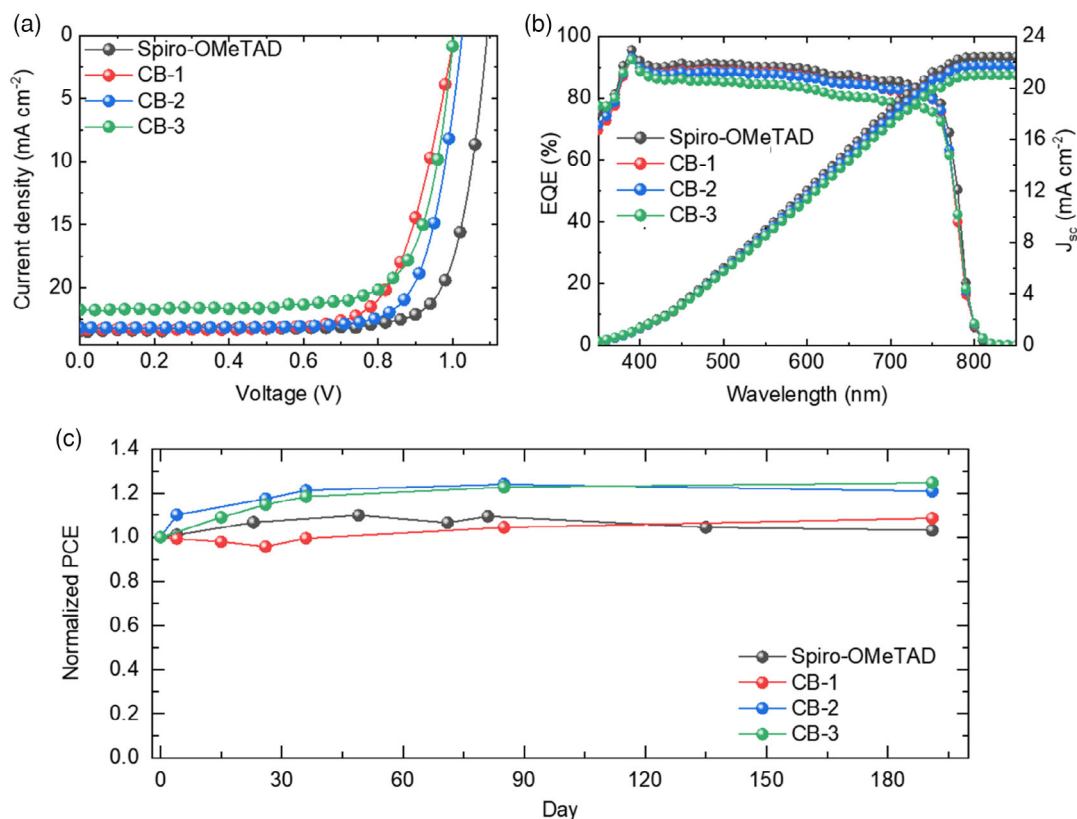


Figure 5. a) J - V curves of champion PSCs under reverse scan direction and b) EQE spectra of the devices using CB-1, CB-2, CB-3, and spiro-OMeTAD as HTMs. c) long-term air-storage stability of PSCs under constant 1 sun illumination using spiro-OMeTAD and CB series as an HTM.

spiro-OMeTAD showed a PCE of 20.26% (Figure 5a). However, the PSCs using CB-1 and CB-3 exhibited lower PCEs; the PSC using CB-1 showed a PCE of 16.78% having V_{oc} of 1.004 V, J_{sc} of 23.31 mA cm⁻², and FF of 0.717 and CB-3 showed a PCE of 16.74% having V_{oc} of 1.003 V, J_{sc} of 22.35 mA cm⁻², and FF of 0.747 in each champion device. The highest PCE of the devices using CB-2 can be attributed to the effective defect passivation by the fluorine atom, which can interact with the undercoordinated Pb²⁺ in the perovskite.^[44,47–49] In addition, the highly planar molecular configuration might particularly improve V_{oc} based on the increase in the molecular ionization potential, thereby increasing built-in potential of the device.^[50] Furthermore, the strong intermolecular π - π interaction based on the molecular planarity can contribute to the improvement in FF by decreasing the interfacial resistance. On the other hand, the degradation in the device performance using CB-1 might result from the absence of the passivation effect as well as the inhomogeneous film morphology despite its high conductivity and hole mobility (Figure 3a). Although CB-3 exhibited the passivation effect and a deeper HOMO level with the presence of trifluoromethyl group, the lowest film conductivity and hole mobility only allowed the limited J_{sc} , and the non-planarity and its poor macroscopic film morphology with the aggregates allowed limited V_{oc} , resulting in the lowest PCE among the devices. We also measured external quantum efficiency (EQE) of the devices and the integrated J_{sc} exhibited a consistent trend and

Table 2. Photovoltaic performance of the champion PSCs based on CB-1, CB-2 and CB-3 and spiro-OMeTAD.

| HTM | V_{oc} [V] | J_{sc} [mA cm ⁻²] | J_{sc} from EQE [mA cm ⁻²] | FF | PCE [%] |
|--------------|--------------|---------------------------------|--|-------|---------|
| CB-1 | 1.004 | 23.31 | 21.73 | 0.717 | 16.78 |
| CB-2 | 1.025 | 23.19 | 21.74 | 0.767 | 18.23 |
| CB-3 | 1.003 | 22.35 | 20.98 | 0.747 | 16.74 |
| spiro-OMeTAD | 1.092 | 23.43 | 22.41 | 0.792 | 20.26 |

value with that of the J - V curves (Figure 5b). Detailed photovoltaic parameters are summarized in Table 2 and also the statistics of 20 individual devices for each HTM are presented in Figure S20, Supporting Information. Furthermore, we investigated the hysteresis behavior of the devices using the HTMs with a definition of hysteresis index (HI) as $\frac{PCE_{reverse} - PCE_{forward}}{PCE_{reverse}}$ (Figure S21, Supporting Information).^[42] While the control device using spiro-OMeTAD exhibited decent J - V hysteresis characteristic with a HI of 5.8%, the devices using CB HTMs resulted in higher HIs as 24.3%, 22.8%, and 13.3% for CB-1, CB-2, and CB-3, respectively. We may attribute the prominent hysteresis of the devices to the thinness of the HTMs that can be relatively more subject to the impact of ion migration

compared to spiro-OMeTAD on the perovskite layer (Figure S16 and S19, Supporting Information).

We carried out the long-term air-storage stability test of the devices without encapsulation that have been stored in dark under the relative humidity below 10% (Figure 5c). All the devices basically proved being super stable with the use of the CB HTMs and not showing a degradation of PCEs over 6 months. The normalized PCEs of the device using CB-2 (121%) or CB-3 (125%) were higher than that of the device using spiro-OMeTAD (103%), which can be ascribed to the fluorine-containing functional groups of CB-2 and CB-3. Although the device using CB-1 showed slightly lower normalized PCEs than that using CB-2 or CB-3, it was still comparable to the device using spiro-OMeTAD by maintaining almost 109% of its initial PCE over 6 months. Also, we measured the steady-state efficiency of the champion devices using spiro-OMeTAD or CB-2 by tracking maximum power point (MPP) after 16 months of storage. At 100 s of the MPP tracking, the steady-state efficiency was 18.75% and 16.02% for the PSCs using spiro-OMeTAD and CB-2, respectively (Figure S22, Supporting Information).

To investigate the excellent stability of the devices having the CB HTMs, we measured a water contact angle of the HTMs deposited on the perovskite (Figure S23, Supporting Information). The water contact angle of CB-1, CB-2, and CB-3 were 67.9°, 88.9°, and 101.8°, respectively, which were larger than that of spiro-OMeTAD (64.6°). Especially, the much larger contact angles of CB-2 and CB-3 indicated their strong hydrophobicity that arose from the fluorophenyl and trifluoromethylphenyl, respectively.^[35] The superior hydrophobicity of CB-2 and CB-3 can effectively prevent moisture penetration into the perovskite layer leading to superior device stability.

3. Conclusion

We successfully designed and synthesized three BDP core-based organic HTMs, CB-1, CB-2, and CB-3, and demonstrated efficient and stable PSCs using the HTMs. The BDP core unit was functionalized by 4-methoxyphenyl, 3-fluorophenyl, and 3-trifluoromethylphenyl, respectively, that intended passivation of defects in perovskites. The molecules were examined by various characterization methods in terms of electrochemical, optical, thermal, electronic, and optoelectronic properties. Our results presented that the functionalization of the BDP unit can lead to the effective defect passivation and molecular planarity according to the substituents. We found out that the fluorinated derivatives of CB-2 and CB-3 can suppress non-radiative recombination at the interface indicated by the PL characteristics, which can be attributed to the passivation of the undercoordinated Pb²⁺ by fluorine. MD simulations also verified the passivation interactions of fluorinated CB-2 and CB-3 with the Pb atoms of the perovskite. Also, the molecular planarity of CB-2 was confirmed by the simulation and the calculation of small dihedral angle between the BDP unit and the 3-fluorophenyl of CB-2, which can lead to the intermolecular π - π interaction and thus facilitate the hole extraction. Therefore, the PSC using CB-2 achieved the highest PCE of 18.23%. However, CB-3 showed the lower PCE of 16.74% because of the inferior hole-transporting capability and non-planar molecular configuration

despite the passivation effect. Also, CB-1 without the passivation effect resulted in the lower PCE of 16.78% despite the high mobility and film conductivity. Furthermore, the molecular hydrophobicity of the fluorinated HTMs enabled the devices to demonstrate excellent long-term storage stability in the air without encapsulation and showed no degradation of their PCEs over 6 months. We believe this study provides a prospect for future materials design of efficient and highly stable HTMs by enriching the chemistry of BDP-based organic small molecules.

4. Experimental Section

Perovskite Thin-Films and Solar Cells Fabrication: FTO glass substrates were cleaned with acetone and isopropyl alcohol (IPA) to use as a conducting electrode. On the FTO glass substrates, a compact TiO₂ layer was deposited by spray pyrolysis using titanium diisopropoxide bis(acetylacetonate) (Sigma-Aldrich) dissolved in isopropanol (1:15 in volume), which was followed by thermal annealing at 450 °C for 30 min. A mesoporous TiO₂ layer was deposited on top of the compact TiO₂ layer using a diluted TiO₂ paste (Greatcell Solar 30 NR-D) in ethanol (1:9 in volume). The solution was spin-coated at 5000 rpm for 20 s followed by sintering at 500 °C for 30 min. On the mesoporous TiO₂ layer, a SnO₂ layer was formed by spin-coating 0.1 M SnCl₄ solution (Acros) dissolved in water and subsequent annealing at 190 °C for 1 h. To deposit perovskite, the substrates were transferred into a glove box. The perovskite precursor solution was prepared by mixing FAI (1.04 M), PbI₂ (1.19 M), MABr (0.16 M), PbBr₂ (0.16 M), and CsI (0.10 M) in a mixed solvent of DMF:DMSO (78:22 in volume). The solution was spin-coated at 2000 rpm for 10 s followed by 5000 rpm for 30 s. During the high rpm step of the spin-coating, 125 μ L of ethyl acetate was dropped on the substrate. The films were annealed at 100 °C for 60 min. After cooling down the substrates, HTMs were deposited on top of the perovskite layer. About 20 mM of CB series and 63 mM of spiro-OMeTAD were prepared by using chlorobenzene as a solvent. The HTMs were doped with Li-bis (trifluoromethanesulphonyl) imide, FK 209 Co(III) TFSI, and 4-*tert*-butylpyridine at the ratio of 0.53:0.055:0.0033 in molar concentration compared to that of both CBs or spiro-OMeTAD. The devices were completed with 70 nm-thick gold electrodes by thermal evaporation.

Device Characterization: Current density–voltage (J - V) characteristics were measured under 1-sun AM 1.5G illumination generated by Xenon lamp solar simulator (450 W, Oriol Sol3A, AAA class). The light intensity was calibrated using a Si reference equipped with an infrared-cutoff (KG5) filter prior to the measurement. A black mask defined the active area of 0.16 cm² with an aperture of 4 \times 4 mm. The J - V curves were scanned under the scan rate of 100 mV s⁻¹ with 4 s pre-illumination time. During the J - V scan, an external voltage bias was applied and the current response was recorded with a digital source meter (Keithley 2400). The incident photon to current conversion efficiency (IPCE) of the solar cells devices was measured by IQE200B (Oriol).

Photoluminescence: The PL spectra of the perovskite thin films were acquired using FluoroLog, Horiba Jobin Yvon fluorescence spectrometer upon excitation at 625 nm for the steady-state PL measurement and 635 nm for the transient PL measurement.

Scanning Electron Microscopy: The top-view and cross-section images were obtained using FEI Teneo scanning electron microscope. The measurements were performed under the accelerating voltage of 2–3 kV. In lens detector and Everhart–Thornley detector were used to acquire the cross-section and top-view images, respectively.

Lateral Conductivity: Conductivity measurement of BDP-based HTMs and spiro-OMeTAD were carried out using the OFET configuration with two-contact electrical conductivity set-up. The OFET substrates were purchased from Fraunhofer IPMS. The substrates were prepared first washing with acetone and ethanol then with 20 min oxygen plasma cleaning. BDP-based HTMs and spiro-OMeTAD were deposited from a chlorobenzene

solution (20 and 63 mM, respectively) chemically doped with FK-209, Li-TFSI, and *t*-BP as additives by spin-coating (at 4000 rpm for 30 s). Conductivity measurements were carried out on the 2.5 μm channel by sweeping from -10 to 10 V (source-drain voltage) at a scan rate of 1 V s^{-1} with a Keithley 2612 A. The data were recorded with the KickStart software program. The channel width and height are 10 and 40 nm, respectively, and the gate capacity is 15 nF. The conductivity was calculated from linear fit of the current–voltage measurement and Ohm's law.

Hole-Drift Mobility: The XTOF technique was used to characterize charge transport in the films of CB-1, CB-2, and CB-3 transporting materials (HTM). Samples are prepared under drop casting technique on Al-coated glass plates using CB as solvent, sample thickness was 0.54–1.2 μm . The corona charging used to create electric fields in the HTM layer. Charge carriers were generated at the layer surface by illumination with pulses of nitrogen laser (pulse duration was 1 ns and wavelength 337 nm). The layer surface potential decrease as a result of pulse illumination was about 5% of initial potential and so was ensured small-charge mode in XTOF measurement. The capacitance probe deposited over the sample and connected to the wide-frequency-band electrometer measured the speed of the surface potential decrease dU/dt , which is equivalent to a current in widely known TOF technique. The transit time t_t was determined by the kink on the curve of the dU/dt transient in double logarithmic plot and investigated materials are characterized by dispersive hole transport. The drift mobility was calculated by the formula $\mu_0 = d^2 / U_0 t_t$, where d is the layer thickness and U_0 is the surface potential at the moment of illumination.

Water-Contact Angle: Water-contact angle on the top of thin layers of BDP-based HTMs was measured using the KRUS DSA100 optical contact angle instrument. Measurements were conducted using the sessile drop program with 0.5 mm needle size. Drops of water at a rate of 0.01 mL min^{-1} and a volume of $12\text{ }\mu\text{L}$ were created. Substrates were prepared by spin coating 20 mM HTM solutions onto perovskite layers. The image was recorded 1 s after the interaction of the water drop with the HTM layer.

Computational Details: All calculations are performed within the DFT, as implemented in CP2K code.^[51] The atomic DZVP-MOLOPT atomic basis set, auxiliary plane wave basis set with 450 Ry cutoff for the isolated molecules and 600 Ry for interfaces, as well as Goedecker–Teter–Hutter (GTH) pseudopotentials have been employed in the calculations.^[52,53] The interactions at the interface have been studied using Perdew–Burke–Ernzerhof (PBE) density functional including Grimme's dispersion correction, required for the description of non-covalent interactions at the interface.^[54,55] To ensure the consistency of the description, the bulk perovskite cell parameters corresponding to stoichiometry $([\text{FAPbI}_3]_{0.87}[\text{MAPbBr}_3]_{0.13})_{0.92}(\text{CsPbI}_3)_{0.08}$ and atomic positions were optimized at PBE-D3 level of theory as well. The energy and spatial distribution of frontier molecular orbitals of CB-1, CB-2, and CB-3 were analyzed using PBE-D3, B3LYP, and PBE0 density functionals. To accelerate hybrid functional calculations, auxiliary density matrix method (ADMM) is used.^[56] Structures were visualized with visualization for electronic and structural analysis and visual molecular dynamics codes.^[57,58]

Supporting Information

Supporting Information is available from the Wiley Online Library or from the author.

Acknowledgements

The authors acknowledge the Swiss National Science Foundation (SNSF) funding through the Synergia Grant EPISODE (Grant No. CRSII5_171000). This project has received funding from the European Union's Horizon 2020 research and innovation program under grant agreement No. 763989 APOLO. This research was supported by Basic Science Research Program through the National Research Foundation of Korea

(NRF) funded by the Ministry of Education (2020R1A6A3A03038147). The authors extend their appreciation to the Deputyship for Research & Innovation, Ministry of Education in Saudi Arabia for funding this research work through the project number 526. We acknowledge Professor Raffaella Buonsanti for the use of the Fluorolog system and Professor Hubert Girault for the use of the water contact-angle measurement system. The research is carried out using the equipment of the shared research facilities of HPC computing resources at Lomonosov Moscow State University.

Open access funding provided by Ecole Polytechnique Federale de Lausanne.

Conflict of Interest

The authors declare no conflict of interest.

Data Availability Statement

Research data are not shared.

Keywords

benzodipyrrole, defect passivation, hole-transporting materials, molecular planarity, perovskite solar cells

Received: August 21, 2021

Revised: November 10, 2021

Published online:

- [1] N. G. Park, M. Grätzel, T. Miyasaka, K. Zhu, K. Emery, *Nat. Energy* **2016**, *1*, 16152.
- [2] W. S. Yang, J. H. Noh, N. J. Jeon, Y. C. Kim, S. Ryu, J. Seo, S. I. Seok, *Science* **2015**, *348*, 1234.
- [3] Q. Dong, Y. Fang, Y. Shao, P. Mulligan, J. Qiu, L. Cao, J. Huang, *Science* **2015**, *347*, 967.
- [4] S. D. Stranks, G. E. Eperon, G. Grancini, C. Menelaou, M. J. Alcocer, T. Leijtens, L. M. Herz, A. Petrozza, H. J. Snaith, *Science* **2013**, *342*, 341.
- [5] J. H. Heo, S. H. Im, J. H. Noh, T. N. Mandal, C.-S. Lim, J. A. Chang, Y. H. Lee, H.-J. Kim, A. Sarkar, M. K. Nazeeruddin, M. Grätzel, S. I. Seok, *Nat. Photonics* **2013**, *7*, 486.
- [6] *NREL Research Cell Record Efficiency Chart*, <https://www.nrel.gov/pv/assets/pdfs/best-research-cellefficiencies.20200925.pdf> (accessed: August 2021).
- [7] A. Kojima, K. Teshima, Y. Shirai, T. Miyasaka, *J. Am. Chem. Soc.* **2009**, *131*, 6050.
- [8] J. J. Yoo, G. Seo, M. R. Chua, T. G. Park, Y. Lu, F. Rotermund, Y.-K. Kim, C. S. Moon, N. J. Jeon, J.-P. Correa-Baena, V. Bulović, S. S. Shin, M. G. Bawendi, J. Seo, *Nature* **2021**, *590*, 587.
- [9] G. Grancini, C. Roldán-Carmona, I. Zimmermann, E. Mosconi, X. Lee, D. Martineau, S. Narbey, F. Oswald, F. De Angelis, M. Graetzel, M. K. Nazeeruddin, *Nat. Commun.* **2017**, *8*, 15684.
- [10] X. Zhao, F. Zhang, C. Yi, D. Bi, X. Bi, P. Wei, J. Luo, X. Liu, S. Wang, X. Li, S. M. Zakeeruddin, M. Grätzel, *J. Mater. Chem. A* **2016**, *4*, 16330.
- [11] H. D. Pham, L. Xianqiang, W. Li, S. Manzhos, A. K. K. Kyaw, P. Sonar, *Energy Environ. Sci.* **2019**, *12*, 1177.
- [12] M. L. Petrus, A. Music, A. C. Closs, J. C. Bijleveld, M. T. Sirtl, Y. Hu, T. J. Dingemans, T. Bein, P. Docampo, *J. Mater. Chem. A* **2017**, *5*, 25200.

- [13] Y.-K. Wang, Z.-C. Yuan, G.-Z. Shi, Y.-X. Li, Q. Li, F. Hui, B.-Q. Sun, Z.-Q. Jiang, L.-S. Liao, *Adv. Funct. Mater.* **2016**, *26*, 1375.
- [14] K. Rakstys, C. Igci, M. K. Nazeeruddin, *Chem. Sci.* **2019**, *10*, 6748.
- [15] H. D. Pham, T. C.-J. Yang, S. M. Jain, G. J. Wilson, P. Sonar, *Adv. Energy Mater.* **2020**, *10*, 1903326.
- [16] J. Urieta-Mora, I. García-Benito, A. Molina-Ontoria, N. Martín, *Chem. Soc. Rev.* **2018**, *47*, 8541.
- [17] H. Min, M. Kim, S.-U. Lee, H. Kim, G. Kim, K. Choi, J. H. Lee, S. I. Seok, *Science* **2019**, *366*, 749.
- [18] Q. Jiang, Y. Zhao, X. Zhang, X. Yang, Y. Chen, Z. Chu, Q. Ye, X. Li, Z. Yin, J. You, *Nat. Photonics* **2019**, *13*, 460.
- [19] H. Tsuji, Y. Yokoi, S. Furukawa, E. Nakamura, *Heterocycles* **2015**, *90*, 261.
- [20] H. Tsuji, Y. Yokoi, C. Mitsui, L. Ilies, Y. Sato, E. Nakamura, *Chem. Asian J.* **2009**, *4*, 655.
- [21] G. W. P. Pruisen, E. A. Pidko, M. M. Wienka, R. A. J. Janssen, *J. Mater. Chem. C* **2014**, *2*, 731.
- [22] A. P. Dhondge, Y.-X. Huang, T. Lin, Y.-H. Hsu, S.-L. Tseng, Y.-C. Chang, H. J. H. Chen, M.-Y. Kuo, *J. Org. Chem.* **2019**, *84*, 14061.
- [23] R. Shang, Z. Zhou, H. Nishioka, H. Halim, S. Furukawa, I. Takei, N. Ninomiya, E. Nakamura, *J. Am. Chem. Soc.* **2018**, *140*, 5018.
- [24] Z. Zhou, Z. Qiang, T. Sakamaki, I. Takei, R. Shang, E. Nakamura, *ACS Appl. Mater. Interfaces* **2019**, *11*, 22603.
- [25] T. Nakamura, S. Furukawa, E. Nakamura, *Chem. Asian J.* **2016**, *11*, 2016.
- [26] X. Zhou, F. Kong, Y. Sun, Y. Huang, X. Zhang, R. Ghadari, *J. Energy Chem.* **2020**, *44*, 115.
- [27] Y. Liu, Z. Hong, Q. Chen, H. Chen, W. H. Chang, Y. M. Yang, T. B. Song, Y. Yang, *Adv. Mater.* **2016**, *28*, 440.
- [28] D. Liu, B. Kan, X. Ke, N. Zheng, Z. Xie, D. Lu, Y. Liu, *Adv. Energy Mater.* **2018**, *8*, 1801618.
- [29] H. Yao, Y. Cui, R. Yu, B. Gao, H. Zhang, J. Hou, *Angew. Chem., Int. Ed.* **2017**, *56*, 3045.
- [30] X. Ji, T. Zhou, X. Ke, W. Wang, S. Wu, M. Zhang, D. Lu, X. Zhang, Y. Liu, *J. Mater. Chem. A* **2020**, *8*, 5163.
- [31] F. Cai, J. Cai, L. Yang, W. Li, R. S. Gurney, H. Yi, A. Iraqi, D. Liu, T. Wang, *Nano Energy* **2018**, *45*, 28.
- [32] B. X. Zhao, C. Yao, K. Gu, T. Liu, Y. Xiaa, Y.-L. Loo, *Energy Environ. Sci.* **2020**, *13*, 4334.
- [33] M.-H. Jung, *J. Mater. Chem. A* **2019**, *7*, 14689.
- [34] M. Li, J. Wu, G. Wang, B. Wu, Z. Sun, S. Xue, Q. Qiao, M. Liang, *J. Energy Chem.* **2020**, *47*, 10.
- [35] L. Fu, H. Li, L. Wang, R. Yin, B. Li, L. Yin, *Energy Environ. Sci.* **2020**, *13*, 4017.
- [36] I. Cho, N. J. Jeon, O. K. Kwon, D. W. Kim, E. H. Jung, J. H. Noh, J. Seo, S. I. Seok, S. Y. Park, *Chem. Sci.* **2017**, *8*, 734.
- [37] M. Moroni, J. L. Moigne, T. A. Pham, J. Y. Bigot, *Macromolecules* **1997**, *30*, 1964.
- [38] D. Khlaifa, F. Massuyeau, C. P. Ewels, J.-L. Duvail, E. Faulques, K. Alimi, *ChemistrySelect* **2017**, *2*, 10082.
- [39] J. Qiu, H. Liu, X. Li, S. Wang, *Chem. Eng. J.* **2020**, *387*, 123965.
- [40] Y. L. Liao, W. Y. Hung, T. H. Hou, C. Y. Lin, K. T. Wong, *Chem. Mater.* **2007**, *19*, 6350.
- [41] P. Gratia, A. Magomedov, T. Malinauskas, M. Daskeviciene, A. Abate, S. Ahmad, M. Grätzel, V. Getautis, M. K. Nazeeruddin, *Angew. Chem., Int. Ed.* **2015**, *54*, 11409.
- [42] H. Kim, M. Pei, Y. Lee, A. A. Sutanto, S. Paek, V. I. E. Queloz, A. J. Huckaba, K. T. Cho, H. J. Yun, H. Yang, M. K. Nazeeruddin, *Adv. Funct. Mater.* **2020**, *30*, 1910620.
- [43] N. Li, S. Tao, Y. Chen, X. Niu, C. K. Onwudinanti, C. Hu, Z. Qiu, Z. Xu, G. Zheng, L. Wang, Y. Zhang, L. Li, H. Liu, Y. Lun, J. Hong, X. Wang, Y. Liu, H. Xie, Y. Gao, Y. Bai, S. Yang, G. Brocks, Q. Chen, H. Zhou, *Nat. Energy* **2019**, *4*, 408.
- [44] H. Li, L. Tao, F. Huang, Q. Sun, X. Zhao, J. Han, Y. Shen, M. Wang, *ACS Appl. Mater. Interfaces* **2017**, *9*, 38967.
- [45] H. Kanda, O. J. Usiobo, C. Momblona, M. Abuhelaiqa, A. A. Sutanto, C. Igci, X.-X. Gao, J.-N. Audinot, T. Wirtz, M. K. Nazeeruddin, *Sol. RRL* **2021**, *5*, 2000650.
- [46] M. Stolterfoht, C. M. Wolff, J. A. Márquez, S. Zhang, C. J. Hages, D. Rothhardt, S. Albrecht, P. L. Burn, P. Meredith, T. Unold, D. Neher, *Nat. Energy* **2018**, *3*, 847.
- [47] Y. K. Wang, H. Ma, Q. Chen, Q. Sun, Z. Liu, Z. Sun, X. Jia, Y. Zhu, S. Zhang, J. Zhang, N. Yuan, J. Ding, Y. Zhou, B. Song, Y. Li, *ACS Appl. Mater. Interfaces* **2021**, *13*, 7705.
- [48] S.-C. Chen, D. Wang, Q. Zheng, *Sol. RRL* **2020**, *4*, 2000321.
- [49] X. Li, W. Li, Y. Yang, X. Lai, Q. Su, D. Wu, G. Li, K. Wang, S. Chen, X. W. Sun, A. K. K. Kyaw, *Sol. RRL* **2019**, *3*, 1900029.
- [50] Y. Dong, V. C. Nikolis, F. Talmack, Y.-C. Chin, J. Benduhn, G. Londi, J. Kublitski, X. Zheng, S. C. B. Mannsfeld, D. Spoltore, L. Muccioli, J. Li, X. Blase, D. Beljonne, J.-S. Kim, A. A. Bakulin, G. D'Avino, J. R. Durrant, K. Vandewal, *Nat. Commun.* **2020**, *11*, 4617.
- [51] T. D. Kühne, M. Iannuzzi, M. Del Ben, V. V. Rybkin, P. Seewald, F. Stein, T. Laino, R. Z. Khaliullin, O. Schütt, F. Schiffmann, D. Golze, J. Wilhelm, S. Chulkov, M. H. Bani-Hashemian, V. Weber, U. Borštnik, M. Taillefumier, A. S. Jakobovits, A. Lazzaro, H. Pabst, T. Müller, R. Schade, M. Guidon, S. Andermatt, N. Holmberg, G. K. Schenter, A. Hehn, A. Bussy, F. Belleflamme, G. Tabacchi, et al., *J. Chem. Phys.* **2020**, *152*, 194103.
- [52] J. VandeVondele, J. Hutter, *J. Chem. Phys.* **2007**, *127*, 114105.
- [53] S. Goedecker, M. Teter, J. Hutter, *Phys. Rev. B* **1996**, *54*, 1703.
- [54] J. P. Perdew, K. Burke, M. Ernzerhof, *Phys. Rev. Lett.* **1996**, *77*, 3865.
- [55] S. Grimme, J. Antony, S. Ehrlich, H. Krieg, *J. Chem. Phys.* **2010**, *132*.
- [56] M. Guidon, J. Hutter, J. VandeVondele, *J. Chem. Theory Comput.* **2010**, *6*, 2348.
- [57] K. Momma, F. Izumi, *J. Appl. Crystallogr.* **2011**, *44*, 1272.
- [58] W. Humphrey, A. Dalke, K. Schulten, *J. Mol. Graph.* **1996**, *14*, 33.